Available online at www.sciencedirect.com
ScienceDirect
C. R. Physique 7 (2006) 501–508
COMPTES RENDUS PHYSIQUE
http://france.elsevier.com/direct/COMREN/

Electromagnetic modelling/Modélisation électromagnétique

Realistic numerical modelling of human head tissue exposure to electromagnetic waves from cellular phones

Gilles Scarella [a], Olivier Clatz [b], Stéphane Lanteri [a], Grégory Beaume [a], Steve Oudot [b], Jean-Philippe Pons [c], Sergo Piperno [a,*], Patrick Joly [b], Joe Wiart [d]

[a] *Cermics, ENPC, INRIA, 6 et 8 avenue Blaise Pascal, Cité Descartes, Champs sur Marne, 77455 Marne la Vallée cedex 2, France*
[b] *INRIA, 2004, route des lucioles, BP 93, 06902 Sophia Antipolis, France*
[c] *Certis, ENPC, INRIA, 6 et 8 avenue Blaise Pascal, Cité Descartes, Champs sur Marne, 77455 Marne la Vallée cedex 2, France*
[d] *France Télécom Research & Development, 92794 Issy-les-Moulineaux, France*

Available online 22 June 2006

Abstract

The ever-rising diffusion of cellular phones has brought about an increased concern for the possible consequences of electromagnetic radiation on human health. Possible thermal effects have been investigated, via experimentation or simulation, by several research projects in the last decade. Concerning numerical modeling, the power absorption in a user's head is generally computed using discretized models built from clinical MRI data. The vast majority of such numerical studies have been conducted using Finite Differences Time Domain methods, although strong limitations of their accuracy are due to heterogeneity, poor definition of the detailed structures of head tissues (staircasing effects), etc. In order to propose numerical modeling using Finite Element or Discontinuous Galerkin Time Domain methods, reliable automated tools for the unstructured discretization of human heads are also needed. Results presented in this article aim at filling the gap between human head MRI images and the accurate numerical modeling of wave propagation in biological tissues and its thermal effects. ***To cite this article: G. Scarella et al., C. R. Physique 7 (2006).***

Résumé

Modélisation numérique réaliste des effets électromagnétiques des téléphones mobiles. La diffusion croissante des téléphones mobiles rend nécessaire des études précises des effets des ondes émises sur les utilisateurs. Les effets thermiques ont été majoritairement simulés numériquement à partir d'images médicales issues de scanners et de méthodes de différences finies sur grilles cartésiennes, malgré leur faible précision sur des matériaux hautement hétérogènes. Peu d'études s'appuyant sur des reconstructions précises des structures externes et internes des tissus de la tête d'une part, et d'autre part sur des méthodes numériques s'appuyant sur des maillages non-structurés de type éléments finis ont été menées, car la chaine permettant d'obtenir une discrétisation non-structurée à partir d'images médicales manque cruellement. Les résultats présentés ici illustrent quelques avancées récentes dans la génération de maillages non-structurés à partir d'images médicales et dans les calculs utilisant des éléments finis discontinus, tout en comportant quelques aspects prospectifs sur les effets thermiques. ***Pour citer cet article : G. Scarella et al., C. R. Physique 7 (2006).***

* Corresponding author.
E-mail addresses: stephane.lanteri@sophia.inria.fr (S. Lanteri), serge.piperno@cermics.enpc.fr (S. Piperno).

1631-0705/$ – see front matter
doi:10.1016/j.crhy.2006.03.002

Keywords: Electromagnetic waves; Heterogeneous tissue; Thermal effects; Medical imaging; Unstructured mesh generation; Discontinuous Galerkin methods

Mots-clés : Électromagnétisme ; Tissus hétérogènes ; Imagerie médicale ; Génération de maillages non-structurés ; Méthodes de type Galerkine discontinu

1. Introduction

The diffusion of mobile phones has brought about an increased concern for the possible consequences of electromagnetic radiation on human health, in particular for children. As a matter of fact, when a cellular phone is in use, the transmitting antenna is placed very close to the user's head where a substantial part of the radiated power is absorbed. In the last decade, several research projects have been conducted in order to evaluate the possible biological effects resulting from human exposure to such an electromagnetic radiation [1]. In this context, it is widely accepted that a distinction must be made between thermal and non-thermal biological effects.

Thermal biological effects of microwave radiation have been investigated both from the experimental and numerical viewpoints. Concerning numerical modeling, the power absorption in a user head is generally computed using discretized models built from clinical Magnetic Resonance Imaging (MRI) data. The majority of such numerical studies have been conducted using the widely known Finite Difference Time Domain (FDTD) method [2] for solving the time domain Maxwell equations. In this method, the whole computational domain is discretized using a structured Cartesian grid, which can be directly derived from the structure of MRI images. Due to the possible straightforward implementation of the algorithm and the availability of computational power, the FDTD method is currently the leading method for numerical assessment of human exposure to electromagnetic waves. However, limitations are still seen, due to the rather difficult departure from the commonly used rectilinear grid and cell size limitations regarding very detailed structures of head tissues as well as of a handset which might be essential for reliable compliance testing. So far, little attention has been put to the application of numerical methods able to deal with unstructured grids, i.e., Finite Element, Finite Volume or Discontinuous Galerkin Time Domain (respectively FETD, FVTD, DGTD) methods. This situation is essentially due to the lack of reliable automated tools for the unstructured discretization of human heads.

The HEADEXP project at INRIA (see http://www-sop.inria.fr/caiman/personnel/Stephane.Lanteri/headexp/headexp.html) is aimed at filling the gap between human head MRI images and the efficient and accurate numerical modeling of the interaction of electromagnetic waves emitted by mobile phones on biological tissues. This requires the development of specific image analysis tools and automated unstructured mesh generation tools for the construction of realistic discretized human head models. In this effort, the numerical simulation of the propagation of electromagnetic waves throughout the head tissue will call for modern unstructured mesh solvers, able to take into account the heterogeneity of the electromagnetic characteristics (conductivity, permittivity, permeability tensors) of the underlying media. Preliminary results for numerical dosimetry (Specific Absorption Rate—or SAR distribution) will be presented. An additional step is made towards biological effect simulation by computing the thermal response as a function of time, starting from the SAR distribution. This will require numerically solving the bioheat or Pennes equation [3]. Comparisons will be made with results from state of the art FDTD methods currently used for such studies and with experimental measurements obtained from appropriate phantoms.

2. From images to numerical simulation

2.1. Segmentation tools

Starting from MRI data or the Visible Human 2.0 project [4], the head tissue has to be segmented. Each voxel of the Cartesian representation of MRI data is recognized as made (mainly) of a single material. This leads to tagged voxels which might correspond to a poor representation of the head tissue geometry. After having decided the relevant number of different materials inside a head (each material having its own electromagnetic characteristics), the different tissues must be segmented and the interfaces between tissues have to be meshed, preferably using unstructured triangles, which will be used as inputs for volumic mesh generators.

Different strategies can be used in order to obtain a smooth and accurate segmentation of head tissue and interface triangulations as well. A first strategy consists in using a 'Marching Cube' algorithm [5] which leads to huge

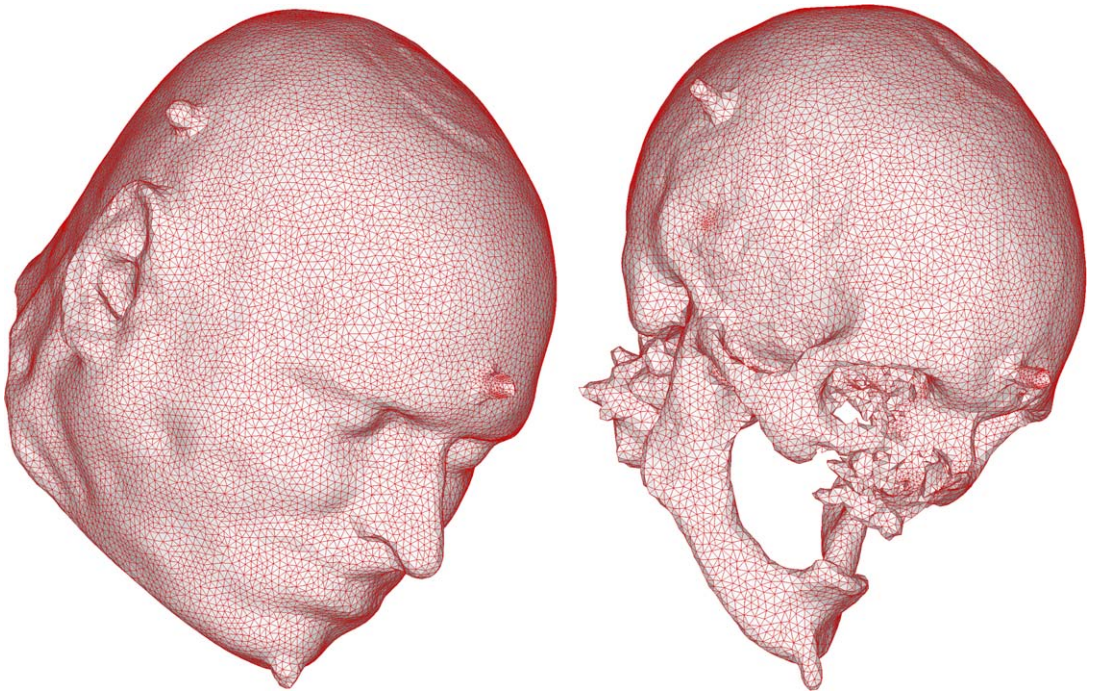

Fig. 1. Triangulated skin (35 000 triangles, $\bar{h} = 3.2$ mm) and skull surface (57 000 triangles, $\bar{h} = 3$ mm).

triangulations of interfaces between segmented subdomains. These triangulations can then be regularized, refined and decimated in order to obtain reasonable surfacic meshes, for example using the tool YAMS [6]. Another strategy consists in using a variant of Chew's algorithm [7], based on Delaunay triangulation restricted to the interface, which allows one to control the size and aspect ratio of interfacial triangles [8]. Examples of the skin and skull surfacic meshes are presented on Fig. 1 ($\bar{h}$ denotes the average edge length). Bumps are artifacts due to the head positioning system in the MRI scanner.

Finally, another very promising strategy deriving from a level-set approach has been tested [9]. The idea is to view segmentation as the definition of contours inside a volumic description of the material. This kind of method can have additional interesting features, like topology preservation for some parts of the tissue (constrained spherical topology, or minimal distance between interfaces). These topological properties can be very important for the volumic meshing tools, and in some cases for some qualitative aspects of the numerical model. Another method, based on 'almost regular tetrahedrizations' can also preserve some topological properties [10] but leads to non-orthogonal staircasing effects.

2.2. *Semi-automatic mesh generation*

The volumic mesh generation is almost automatic. The mesh generator GHS3D [11] is used to mesh volumic domains between triangulated interfaces between materials. The mesh generated is fully unstructured and can lead to some small edges, which is a concern when an explicit time-scheme is used (the stability condition is constrained by the smallest edge or element volume in the mesh). The exterior of the head must also be meshed, up to a certain distance, where an artificial absorbing boundary condition has to be set (in practice, Γ_∞ is a sphere). For numerical simulations with a mobile phone model, the meshing process is a little more complex and requires the meshing of the phone (metallic box with apertures and a dipole model inside) and of the volume between the head, the phone, and the artificial far-field boundary. Tetrahedra are tagged in order to take into account different materials, for which the characteristics are reported in Table 1 (CSF stands for Cerebro-Spinal Fluid). For all tissues, the relative magnetic permeability is set to one, while the variations of the relative electric permittivity ε_r (and thus for the wave velocity) explain how important it can be to take into account accurately heterogeneities in the materials. We present here numerical results obtained for a simplified phone model with the four tissues (skin, skull, CSF, and brain).

Table 1
Relative parameters ε_r and μ_r, conductivity σ, density ρ, and wavelength λ at 1800 MHz

Tissue	ε_r	μ_r	σ (S/m)	ρ (kg/m^3)	λ (mm)
Skin	43.85	1	1.23	1100.	26.73
Skull	15.56	1	0.43	1200.	42.25
CSF	67.20	1	2.92	1000.	20.33
Brain	43.55	1	1.15	1050.	25.26

2.3. Numerical methods

We have chosen to use a Finite Volume Time-Domain solver (MAXDG0), [12] developed in the Caiman project-team at INRIA Sophia Antipolis. It is based on totally centered numerical fluxes at element interfaces and on an explicit leap-frog time-scheme. A $\mathbb{P}_1$-DGTD version of the software exists and a generic high-order capable version is under development, similar to other existing software [13]. The FVTD solver is quite fast and an interesting result of these preliminary study is the evaluation of the accuracy of numerical results obtained on automatically generated unstructured meshes, for highly heterogeneous materials. We should recall here that, for explicit FVTD solvers—and for explicit DGTD solvers as well—the maximal time step required in order to achieve stability is directly related to the smallest elements of the mesh, even if the mesh is only locally refined. Some ongoing works are aimed at dealing with local time-stepping (which is not obvious for reversible leap-frog-type time-schemes) or with locally implicit time-schemes.

For the sake of completeness, we give here the main ideas in the construction of Discontinuous Galerkin methods. These ideas are well known and often presented in a rather mixed finite element approach (with penalization of jumps across elements edges). We propose here another presentation of the method, closer to a higher-order generalization of Finite Volume methods. As usual, we assume we dispose of a partition of a polyhedral domain Ω_h into a finite number of tetrahedra (it could be variable polyhedra). For each element $\mathcal{T}_i$, ε_i and μ_i denote respectively the local electric permittivity and magnetic permeability of the medium (which could be tensors and varying inside the elements). For each internal face $a_{ik} = \mathcal{T}_i \cap \mathcal{T}_k$, let $\boldsymbol{n}_{ik}$ denote the unitary normal, oriented from $\mathcal{T}_i$ towards $\mathcal{T}_k$. Finally, we denote by $\mathcal{V}_i$ the set of indices of elements neighboring $\mathcal{T}_i$. Inside each finite element, the electric and magnetic fields are sought for as linear combinations $(\mathbf{E}_i, \mathbf{H}_i)$ of linearly independent vector fields $\boldsymbol{\varphi}_{ij}, 1 \leqslant j \leqslant d_i$, where d_i denotes the local number of scalar degrees of freedom inside the element $\mathcal{T}_i$ (we denote by $\mathcal{P}_i = \mathrm{Span}(\boldsymbol{\varphi}_{ij}, 1 \leqslant j \leqslant d_i)$). The approximate fields $(\mathbf{E}_h, \mathbf{H}_h)$, defined by $(\forall i, \mathbf{E}_{h|\mathcal{T}_i} = \mathbf{E}_i, \mathbf{H}_{h|\mathcal{T}_i} = \mathbf{H}_i)$are allowed to be discontinuous across element boundaries. The main idea consists in writing separately a variational formulation inside each element. Dot-multiplying Maxwell's equations by any given vector field $\boldsymbol{\varphi} \in \mathcal{P}_i$, integrating over $\mathcal{T}_i$ and integrating by parts yields

$$\begin{cases} \varepsilon_i \displaystyle\int_{\mathcal{T}_i} \boldsymbol{\varphi} \cdot \frac{\partial \mathbf{E}}{\partial t} = -\int_{\partial\mathcal{T}_i} \boldsymbol{\varphi} \cdot (\mathbf{H} \times \boldsymbol{n}) + \int_{\mathcal{T}_i} \operatorname{curl} \boldsymbol{\varphi} \cdot \mathbf{H} \\ \mu_i \displaystyle\int_{\mathcal{T}_i} \boldsymbol{\varphi} \cdot \frac{\partial \mathbf{H}}{\partial t} = \int_{\partial\mathcal{T}_i} \boldsymbol{\varphi} \cdot (\mathbf{E} \times \boldsymbol{n}) - \int_{\mathcal{T}_i} \operatorname{curl} \boldsymbol{\varphi} \cdot \mathbf{E} \end{cases} \tag{1}$$

In Eqs. (1), we now replace the exact fields $\mathbf{E}$ and $\mathbf{H}$ by the approximate fields $\mathbf{E}_h$ and $\mathbf{H}_h$ in order to evaluate volume integrals. For integrals over $\partial\mathcal{T}_i$, some additional approximations have to be done since the approximate fields are discontinuous through element faces. In the finite volume literature, it corresponds to choosing numerical fluxes which approximate the electric and magnetic fluxes $\mathbf{H} \times \boldsymbol{n}$ and $\mathbf{E} \times \boldsymbol{n}$ at the interfaces. These numerical fluxes can be based on upwinding [13] (which leads to some numerical dissipation) and we have chosen to use completely centered fluxes, i.e.,

$$\forall i,\ \forall k \in \mathcal{V}_i, \quad \mathbf{E}_{|a_{ik}} \times \boldsymbol{n}_{ik} \simeq \frac{\mathbf{E}_{i|a_{ik}} + \mathbf{E}_{k|a_{ik}}}{2} \times \boldsymbol{n}_{ik}, \quad \mathbf{H}_{|a_{ik}} \times \boldsymbol{n}_{ik} \simeq \frac{\mathbf{H}_{i|a_{ik}} + \mathbf{H}_{k|a_{ik}}}{2} \times \boldsymbol{n}_{ik}$$

which leads to energy conservation when an explicit leap-frog advancing-in-time scheme is used. Because of the discontinuity of fields through faces, the corresponding finite element mass matrix is only block diagonal, which leads to the same kind of computational cost as for an explicit time-scheme.

When the fields are sought for as constants inside elements (one degree of freedom per field component and per element), the DGTD methods reduces to a Finite Volume method. We also considered here the $\mathbb{P}_1$-DGTD version of the method, where the fields are sought for as, at most, first degree polynomials inside elements (four degrees of freedom per field component and per element). We have chosen $\mathbb{P}_0$ and $\mathbb{P}_1$ Lagrange basis functions, for which all volume and surface integrals are exactly evaluated and for which no storage is required for the mass matrix inverse or stiffness matrices. Thus the computational storage is only related to the numerical unknowns.

Concerning boundary conditions, metallic and first-order absorbing boundary conditions are enforced in a weak sense by computing numerical fluxes through boundary faces a_{ik} (i being the index of the boundary element $\mathcal{T}_i$ and k the one of a fictitious neighbor $\mathcal{T}_k$), based on values of fictitious fields $\mathbf{E}_k$ and $\mathbf{H}_k$. For a metallic boundary face a_{ik}, the boundary condition $\boldsymbol{n}_{ik} \times \mathbf{E}_{|a_{ik}} = 0$ is enforced via $\mathbf{E}_{k|a_{ik}} = -\mathbf{E}_{i|a_{ik}}$ and $\mathbf{H}_{k|a_{ik}} = \mathbf{H}_{i|a_{ik}}$, while a first order Silver–Müller absorbing condition is enforced via $\mathbf{H}_{k|a_{ik}} = c_i \epsilon_i \, \boldsymbol{n}_{ik} \times \mathbf{E}_{i|a_{ik}}$ and $\mathbf{E}_{k|a_{ik}} = -c_i \mu_i \, \boldsymbol{n}_{ik} \times \mathbf{H}_{i|a_{ik}}$. These values correspond to upwind fluxes at the absorbing boundary, based on the hyperbolic nature of the global six-component Maxwell system.

3. Numerical results

A first global mesh has been built around the head and the phone and inside a sphere (of radius 30 cm, which sets the farfield boundary between 1λ and 1.5λ). The mesh is made of 520 559 vertices and 3 123 417 tetrahedra. In terms of the total number of unknowns, since in the MAXDG0 solver the degrees of freedom are the average values on a tetrahedron of the components of the electric and magnetic fields, the overall problem size is 18 740 502. The average edge length is 5.4 mm (maximum length: 25 mm, minimum length: 0.3 mm).

We have used a dipolar source located in the simplified phone model (more precisely in the space between the two elements of the phone model: a main metallic box and a parallelepipedic antenna). The transient excitation is a Gaussian pulse modulated by a sinusoid with a central frequency of 1.8 GHz (total emitted power equal to 1 W). Note that at this frequency, the minimal wavelength is obtained in the CSF (20.3 mm) while the maximal wavelength is 166.7 mm (in air). The time step $\Delta t = 0.091$ ps leads to a CPU time of 616 min on a 16 PC cluster (Pentium4@2GHz, Gigabit Ethernet).

3.1. SAR distributions

The quantity of interest involved in the definition of international norms for mobile phones is the Specific Absorption Rate (SAR), defined by $\text{SAR} = \sigma |\boldsymbol{E}|^2/\rho$. We have shown on Fig. 2 (left) the normalized SAR distribution on the skin and on a facial plane cut. The computed total power absorbed by head tissues is $P_{\text{abs}} = 0.795$ W. Indeed, only mean SAR values over tissue balls are used in mobile phone norms. These quantities can also be computed and should be less sensitive to FVTD inaccuracies due to heterogeneities in materials and elements. The normalized SAR distributions after averaging over 5 mm-radius spheres are shown on Fig. 2 (right).

3.2. FVTD versus $\mathbb{P}_1$-DGTD comparisons

In order to estimate the possible gain obtained with more accurate DGTD methods, we have rebuilt two different unstructured meshes (where ad hoc treatment has deleted artifacts related to the fixation system). We have compared (logarithmic scale) the SAR distributions computed respectively with:

- the FVTD method on a mesh with 7 894 172 elements (48 million-unknown computation, with $\bar{h} = 2.13$ mm);
- the $\mathbb{P}_1$-DGTD method on a mesh with 1 862 136 elements (45 million-unknown computation, with $\bar{h} = 4$ mm).

For these two computations, the memory storage required is almost equivalent (we recall it reduces to the numerical unknowns). However, the computational times required was 2 h 46 min for the FVTD computation on the fine mesh and 6 h 32 min for the $\mathbb{P}_1$-DGTD computation on the coarse mesh (on a 32 AMD-Opteron 2 GHz nodes). The CPU time difference is directly related to the maximal admissible Courant number for both methods (between two and three times smaller for the $\mathbb{P}_1$-DGTD method) since the minimal edges in both meshes were similar.

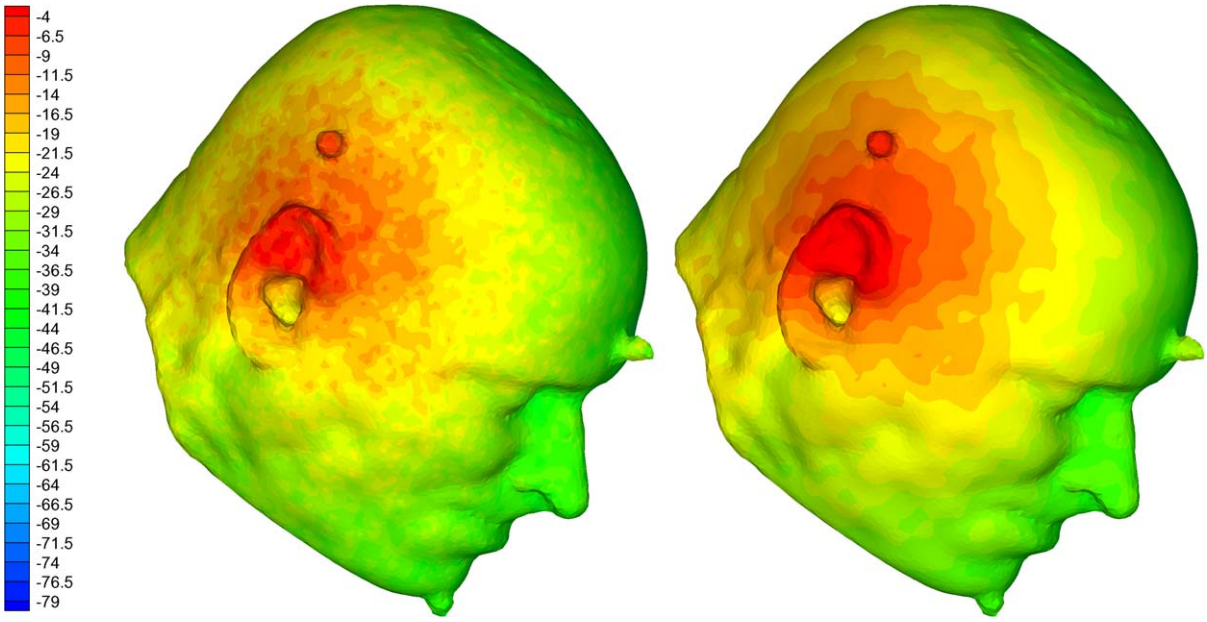

Fig. 2. Distributions of $\mathrm{SAR}(\boldsymbol{x})/\mathrm{SAR}_{\max}$ (left) and 5 mm-sphere averaged normalized SAR (right) in Db.

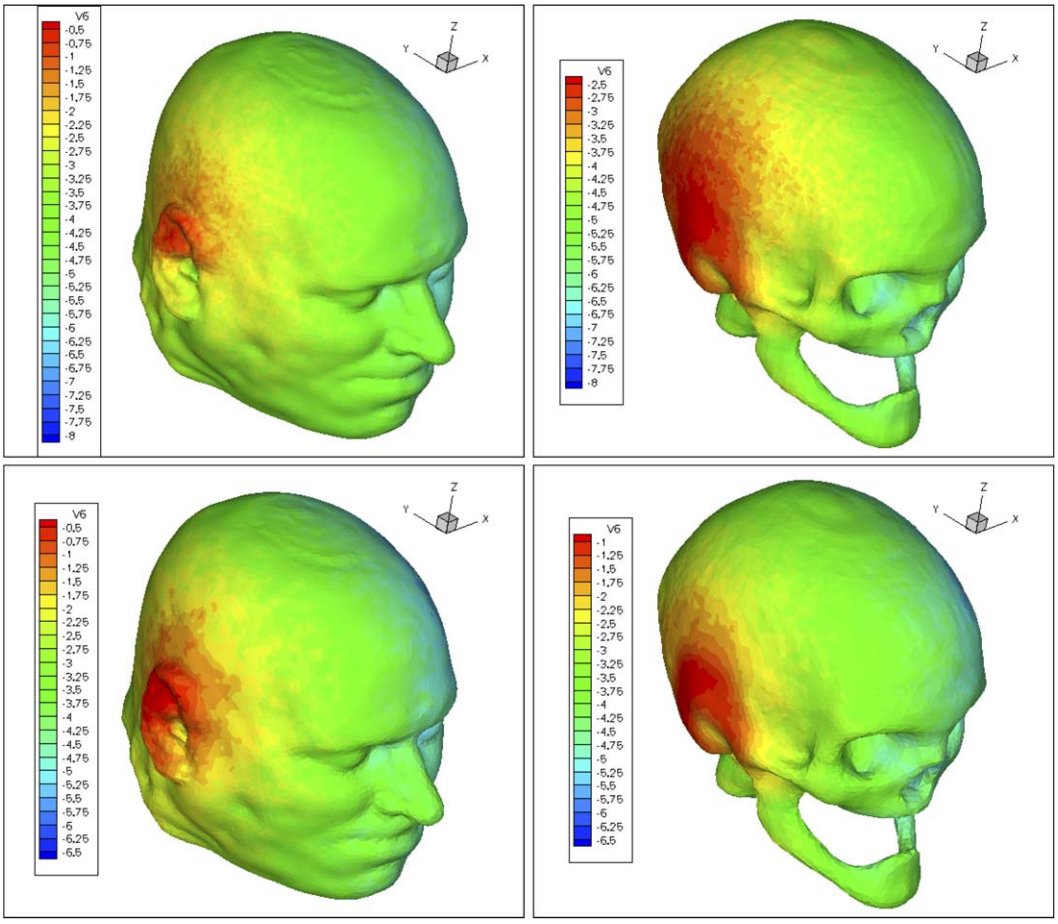

Fig. 3. Distributions of $\mathrm{SAR}(\boldsymbol{x})/\mathrm{SAR}_{\max}$ in Db for the FVTD (top) and the $\mathbb{P}_1$-DGTD (bottom) computations.

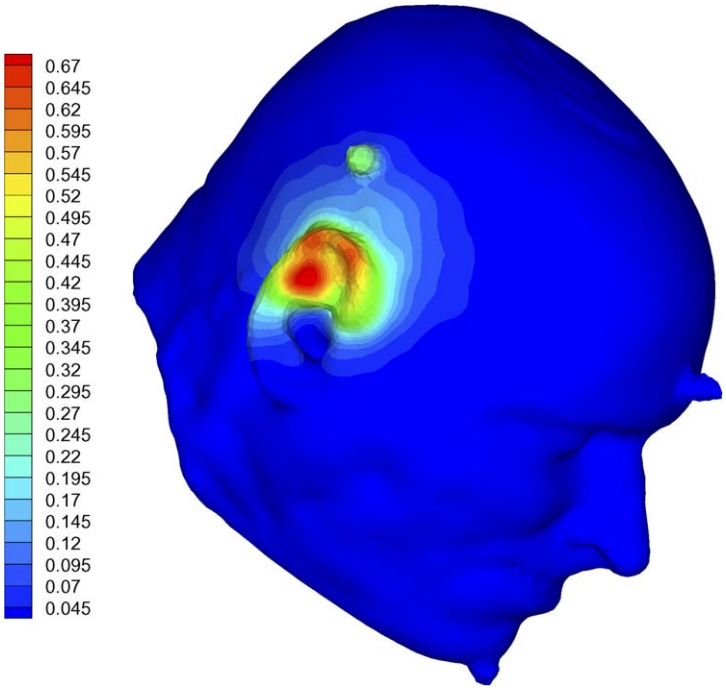

Fig. 4. ΔT due to electromagnetic radiation.

The contour lines on the skin and skull surfaces are shown on Fig. 3. For similar numbers of degrees of freedom, the computed specific absorption rates have different distributions when they are obtained with methods with different orders of accuracy. Therefore, further extensive validations should be done to verify that the FVTD methods converge to similar distributions for finer mesh (it is indeed the case) and to compare the relative efficiencies of $\mathbb{P}_k$-DGTD methods.

3.3. Estimation of thermal increment

The SAR computed can be used as a source term in Pennes bioheat equation, modeling the evolution of the temperature in biological tissue. In the present computation, no convection has been considered and the steady solution is sought for, using a classical P1 Lagrange finite element method. Since the model equation used for the tissue temperature is linear, we can directly obtain the temperature increment ΔT due to electromagnetic radiations (see Fig. 4). In the computation, the averaged-SAR distribution has been used (for which $\bar{\text{SAR}}_{\max} = 38.9$ W/kg). The maximum value less than 1 °C is in good agreement with other studies [14,1].

4. Further works

These preliminary results will be completed in the future with locally-refined tetrahedral meshes, computations with the $\mathbb{P}_k$-DGTD method (at least with $k = 2$) and more realistic mobile phone models. It is clear that the $\mathbb{P}_k$-DGTD methods (with larger k) can provide better accuracy and approximation of the fields. However, they can be competitive only if

(i) the increase in storage and computational time (due to the additional degrees of freedom and the reduction of the admissible time step) can be compensated by the coarsening of the mesh in general, which seems to be true for small k but not indefinitely as k grows; and
(ii) if coarser meshes can be actually used: the construction of coarser meshes which are based on reasonably accurate interfaces between different tissue is not at all obvious and could lead to complex problems in geometrical algorithmics.

Concerning thermal effects, the thermal radiation of the phone and blood convection inside tissues should be taken into account. Many other different aspects should be investigated, not only concerning cellular phones emitted waves but also related to hyperthermia for example.

Acknowledgements

The authors thank INRIA (French National Institute for Computer Science and Automatics, see its home page http://www.inria.fr/) for the support though the research collaborative action HEADEXP (see http://www-sop.inria.fr/caiman/personnel/Stephane.Lanteri/headexp/headexp.html). We wish also to thank all participants not included in the authors list, in particular, Nicholas Ayache, Jean-Daniel Boissonnat, Gary Cohen, Hervé Delingette, Houssem Haddar, Theodore Papadopoulo (INRIA), Jasmine Burguet, Najib Gadi and Isabelle Bloch (ENST), Patrice Brachat, Claude Dedeban (FT R&D, La Turbie), and René De Seze (INERIS).

References

[1] P. Bernardi, M. Cavagnaro, S. Pisa, E. Piuzzi, Specific absorption rate and temperature increases in the head of a cellular phone user, IEEE Trans. Microwave Theory Tech. 48 (2000) 1118–1126.
[2] K.S. Yee, Numerical solution of initial boundary value problems involving Maxwell's equations in isotropic media, IEEE Trans. Antennas and Propagation AP-16 (1966) 302–307.
[3] H.H. Pennes, Analysis of tissue and arterial blood temperature in the resting human forearm, J. Appl. Physiol. 1 (1948) 93–122.
[4] P. Ratiu, B. Hillen, et al., Visible Human 2.0—the next generation, in: Medicine Meets Virtual Reality, vol. 11, IOS Press, 2003, pp. 275–281.
[5] W. Lorensen, H. Cline, Marching cubes: a high resolution 3D surface construction algorithm, in: Siggraph 87, vol. 21, 1987, pp. 163–170.
[6] P. Frey, YAMS, a fully automatic adaptive isotropic surface remeshing procedure, INRIA technical report 0252, 2001.
[7] L.P. Chew, Guaranteed-quality mesh generation for curved surfaces, in: Proc. 9th Annu. ACM Sympos. Comput. Geom., 1993, pp. 274–280.
[8] J.-D. Boissonnat, S. Oudot, Provably good sampling and meshing of surfaces, Graphical Models 67 (5) (2005) 405–451.
[9] O. Faugeras, et al., Variational, geometric and statistical methods for modeling brain anatomy and function, Neuroimage 23 (2004) S46–S55.
[10] J. Burguet, I. Bloch, Homotopic Labeling of Elements in a Tetrahedral Mesh for the Head Modeling, Lect. Notes in Comput. Sci., vol. 3287, Springer-Verlag, Berlin/New York, 2004.
[11] P. Frey, P.-L. George, Mesh Generation, Hermes Science Publications, 2000.
[12] S. Piperno, M. Remaki, L. Fezoui, A non-diffusive finite volume scheme for the 3D Maxwell equations on unstructured meshes, SIAM J. Numer. Anal. 39 (6) (2002) 2089–2108.
[13] J. Hesthaven, T. Warburton, Nodal high-order methods on unstructured grids. I: Time-domain solution of Maxwell's equations, J. Comput. Phys. 181 (1) (2002) 186–221.
[14] O.M.P. Gandhi, Q.X. Li, G. Kang, Temperature rise for the human head for cellular telephones and for peak SARs prescribed in safety guidelines, IEEE Trans. Microwave Theory Tech. 49 (9) (2001) 1607–1613.